Progress In Electromagnetics Research C, Vol. 133, 261–269, 2023

Broadband and High-Efficiency Reflective Linear Polarizer

Xiaojun Huang*, **Xiongwei Ma, Sihan Cui, and Huanhuan Gao**

Abstract—In this paper, we propose a wideband linear polarizer that utilizes metamaterial and metasurface techniques to achieve highly efficient polarization conversion. The proposed polarizer achieves a polarization conversion ratio exceeding 90% at 12.0–16.0 GHz, as confirmed by both simulated and experimental results. The effects of geometric parameters, incidence angle, and polarization angle on the performance of the polarizer are analyzed, and it is demonstrated that the polarizer maintains an extremely high polarization conversion efficiency even under wide-angle incidence. The polarization conversion mechanism is elucidated through the examination of eigenmode and surface current distribution. This work holds significant promise for the control of electromagnetic waves, making it essential for upcoming engineering applications.

1. INTRODUCTION

Metamaterials are artificially fabricated materials that showcase unparalleled electromagnetic (EM) characteristics absent in materials occurring naturally. Among them, metasurfaces (MSs) are two-dimensional structures composed of subwavelength artificial elements arranged periodically with ultrathin physical properties [1]. The utilization of MSs offers several benefits, such as compact size, minimal insertion loss, convenient fabrication and integration, and the capability to modify the behavior of polarization in transmitted and reflected waves [2–5]. As a result, MSs have gained significant attention as a promising research area in the field of metamaterial applications. In this paper, we focus on MS-based polarizers, which possess the capability to change the polarized state of EM waves.

MS-based polarizers can be utilized in two distinct modes: transmission and reflection [6–10]. Three types of polarizers can be distinguished based on the polarized state of EM waves: linear polarizers [11–13], linear to circular polarizers [14], and circular to linear polarizers [15]. A properly designed MS can convert a specific polarization to any arbitrary polarization state. For example, chiral MSs can be created by stacking metallic chiral structures, such as helices, split ring resonance cavities, and other asymmetric configurations, enabling effective control over the polarization state of transmitted waves [16, 17]. Anisotropic MSs are used in the design of reflective polarizers, such as cut-lines, v-shaped resonators, and plasma MSs [18–21].

Recently, a considerable number of polarizers utilizing MSs have been proposed. Reflective linear polarizers, in particular, have emerged as highly prominent polarization devices that have gained widespread adoption. For instance, in [22], a multifunctional polarization converter based on dielectric metamaterial is proposed, achieving linear orthogonal transformation at 11.5–12.6 GHz. In [23], a dual-frequency linear polarizer is introduced, demonstrating effective operation between 3.16–3.52 GHz and 7.19–8.61 GHz in frequency range. The polarizer achieved a remarkable polarization conversion ratio (PCR) exceeding 90%. Furthermore, in [24], a multifunctional metamaterial structure is proposed, which exhibited the capability of achieving convert polarization in both linear and circular.

Received 10 May 2023, Accepted 14 June 2023, Scheduled 23 June 2023

* Corresponding author: Xiaojun Huang (hxj@xust.edu.cn).
The authors are with the College of Communication and Information Engineering, Xi'an University of Science and Technology, Xi'an 710054, China.

The device successfully achieved cross-polarization in three frequency ranges. Despite the significant advancements in polarization conversion achieved by existing polarizers across a broad frequency, much of the research has primarily focused on evaluating their performance under normal incidence of EM waves. Unfortunately, the influence of polarization effects under oblique incidence has been largely overlooked. Therefore, future research should concentrate on investigating the performance of MS-based polarizers under oblique incidence to develop an extensive comprehension of their potential in engineering applications.

In this study, we propose a novel cut-line polarizer based on metasurface technology that exhibits effective polarization conversion of electromagnetic waves over an ultra-wide bandwidth. This advancement holds great significance in the field of manipulating EM wave polarization. The proposed polarizer showcases a remarkable PCR exceeding 0.9 and achieves a relative bandwidth of 28.6% at 12.0–16.0 GHz, enabling efficient cross-conversion of linearly polarized waves. The impact of various factors, including incidence angle, polarization angle, and geometric parameters are analyzed, on the PCR and find that the polarizer's performance is minimally affected by the incidence angle, enabling wide-angle incidence. Analyzing the surface current reveals the basic mechanism of polarization conversion, and the validity of the simulations is confirmed by experimental results. Our study demonstrates the potential of metasurface-based polarizers for achieving ultra-broadband and efficient polarization control of EM waves.

2. SIMULATION AND EXPERIMENTS

Figures 1(a)–(b) illustrate the structure of the proposed MS. The top layer of the MS comprises a cut circle and a rectangular ring, both tilted at a 45° angle on the x-y plane with regard to the x-axis. The bottom-most metal is un-patterned, which prevents EM waves from passing through. The copper layer

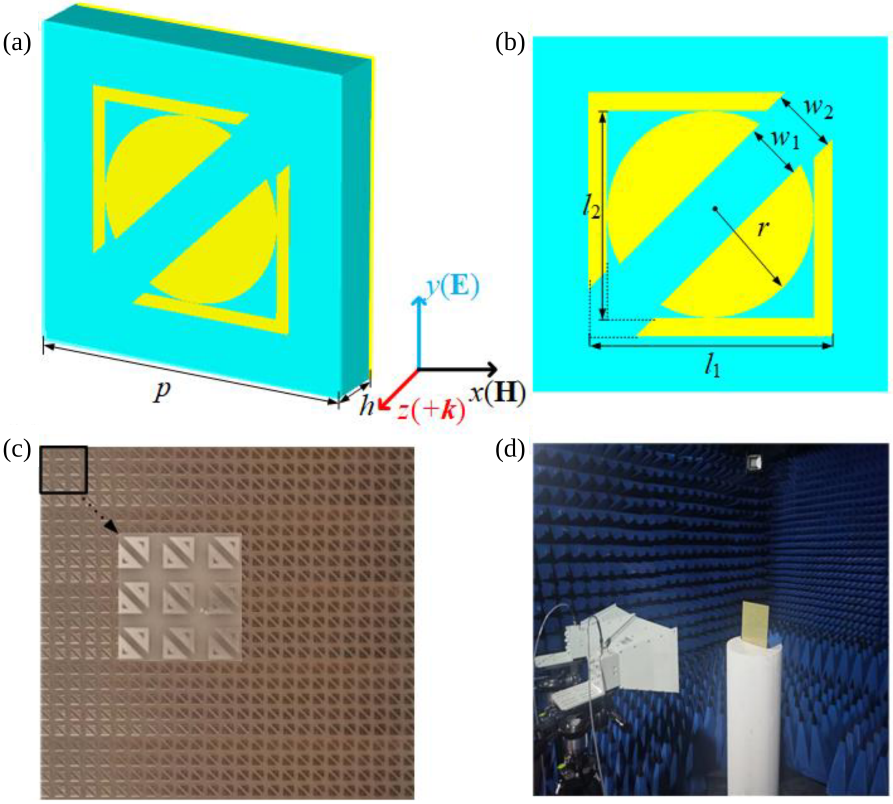

Figure 1. Schematic diagram of MS structure. (a) The side view, (b) the front view, (c) the photograph of the sample, (d) the laboratory environment.

is 0.035 mm thick and has 5.8 10^7 S/m electrical conductivity. The loss tangent and dielectric constant of the FR4 dielectric layer are 0.025 and 4.3, respectively. The optimized geometrical parameters of the MS are as follows: $w_1 = 1.3$ mm, $w_2 = 1.5$ mm, $l_1 = 5.3$ mm, $l_2 = 4.65$ mm, $r = 2.325$ mm, $p = 8$ mm, and $h = 1.5$ mm.

We employ the CST MICROWAVE STUDIO software suite to simulate the MS, utilizing a frequency-domain solver and setting periodic boundary conditions. For experimental verification, we fabricate samples of the MS structure using printed circuit board (PCB) technology, as shown in Fig. 1(c), consisting of a 25 × 25 array of unit cells. As indicated in Fig. 1(d), the experiment requires the use of a network analyzer to measure the reflection coefficients under normal incidence conditions. Two standard horn antennas with operating frequencies of 2–18 GHz are used in the experiment setup. One antenna served as the transmitter of EM waves, while the other acted as the receiver. By adjusting the orientation of the antennas parallel or perpendicular to the ground, various polarized waves can be transmitted or received.

3. RESULTS AND DISCUSSION

Firstly, we examine the characteristics of orthogonally polarized transformation of the device when y-polarized wave is illuminated under the normal incidence. Fig. 2(a) depicts the reflection coefficients of $\mathbf{r}_{yy}$ and $\mathbf{r}_{xy}$ over the frequency range of 11.0–18.0 GHz. Notably, $\mathbf{r}_{xy}$ consistently surpasses -3 dB within the frequency span of 11.6–17.1 GHz. Moreover, $\mathbf{r}_{xy}$ remains above -2 dB throughout the range of 12.0–16.0 GHz, while $\mathbf{r}_{yy}$ remains below -7.5 dB. At the frequency of 13.7 GHz, $\mathbf{r}_{xy}$ reaches its peak value of -0.5 dB. The experimental results are consistent with the simulation ones, offering compelling evidence of the polarizer's exceptional performance in cross-polarization conversion. Fig. 2(b) displays the plot of the PCR within the operating frequency range, defined as [25]: $PCR_y = \frac{|\mathbf{r}_{xy}|^2}{|\mathbf{r}_{xy}|^2+|\mathbf{r}_{yy}|^2}$. The experimental results indicate that the PCR exceeds 0.9 at 12.0–16.0 GHz. The simulations and measurements are in accordance and confirm the highly effective conversion of y- to x-polarization achieved over a broad frequency range. Nevertheless, there is a slight disparity between the simulations and experiments, which can be explained by the following two causes: firstly, the difference in machining accuracy and material parameters should be taken into account. Secondly, because the simulation boundary is infinite, while the fabricated sample is a finite plane, the emitted electromagnetic waves will inevitably undergo electromagnetic edge diffraction, which is also an important factor contributing to the bias.

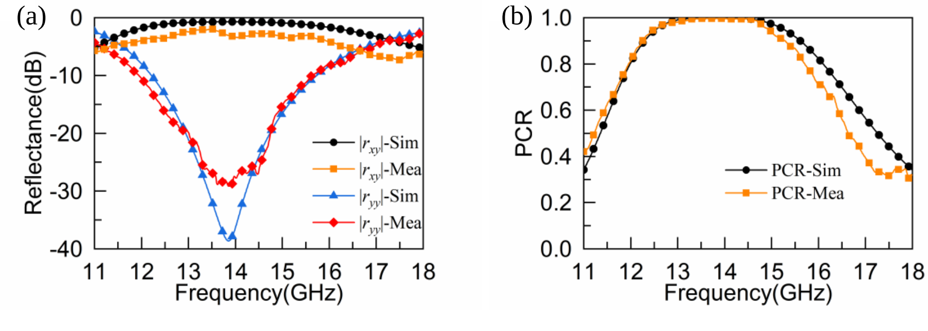

Figure 2. Conversion performance of polarization converter. (a) Reflection coefficient, (b) PCR.

In practical engineering applications, EM waves are incident on objects from various directions, which necessitates studying the polarization conversion properties of electromagnetic metamaterials at oblique angles of incidence. Fig. 3(a) shows the results of polarization deflection for TM waves reflected at different angles of incidence. Based on the simulation results, it can be observed that the designed MS exhibits significant wide-angle oblique incidence characteristics. As depicted in Fig. 3(a), efficient polarization deflection of TM waves can be achieved within a specific bandwidth when the oblique angle of incidence is less than 30°, while maintaining an efficiency level above 0.9. With a gradual increase in the angle of incidence from 30° to 45°, the PCR exhibits a slight decrease while still maintaining a value above 0.8. This observation confirms the favorable characteristics of our polarizer under oblique incidence conditions. In high-frequency region, the gradual redshift of the bandwidth can be primarily attributed to the weakening of the magnetic coupling response between the front and rear metal layers as the angle of incidence increases. This effect is caused by a gradual decrease in the vertical incident surface's decomposed magnetic field component. This decrease in the magnetic field component weakens the resonance between the front and rear metal layers, resulting in a reduction of the high-frequency bandwidth. The MS is designed to enable a specific polarization conversion method. Hence, when the incident polarization orientation of EM wave no longer coincides with the polarization direction that the MS can handle, efficient cross-polarization conversion cannot be achieved. Fig. 3(b) shows that changes in polarization angle significantly impact PCR. This phenomenon occurs because the total intensity of the electric field along the y-axis decreases linearly with the change of polarization angle. Therefore, as the polarization angle increases linearly, the PCR value decreases linearly, eventually reaching 0 when the polarization angle reaches 45°.

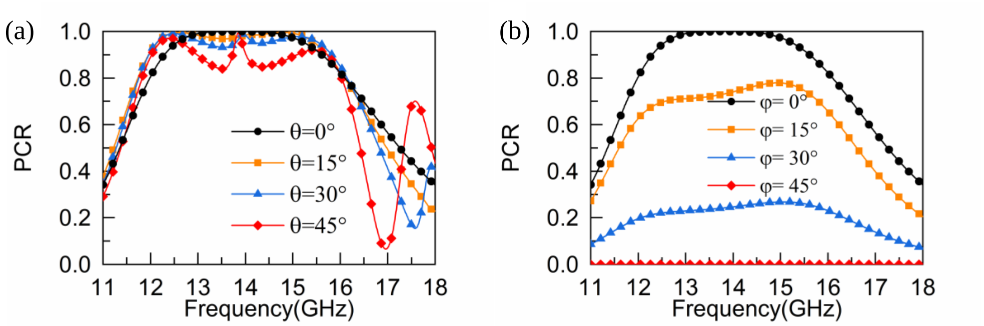

Figure 3. Effects of incident and polarization angle on PCR. (a) Incident angle, (b) polarization angle.

We discuss the influence of geometry on the performance of the designed MS. To ensure accurate analysis results, we maintained constant values for the other parameters when analyzing each parameter. In Fig. 4(a), we illustrate the impact of the period parameter (p) on the PCR. As the period increases from 6 mm to 10 mm, the working frequency band undergoes a blue shift, while the effective working frequency band widens. This increase in bandwidth is due to the increase in resonant size as the period increases. However, the PCR slightly decreases when the period changes from 8 mm to 10 mm, as the coupling between the units is reduced when the resonant size increases. We demonstrate the effects of the dielectric thickness (h) on PCR in Fig. 4(b). Both the high and low frequency ranges undergo linear redshift as h increases. This is because an increase in h enhances the resonance in the structural resonator, causing the working frequency to shift towards the low-frequency band. When h increases to 1.5 mm, PCR approaches 1, but further increases in h result in a significant decrease in PCR due to the strong influence of h on the phase of the EM wave. In Fig. 4(c), we show the change of PCR as the radius parameter (r) increases from 2.31 mm to 2.35 mm. As r increases from 2.31 mm to 2.33 mm, the amplitude and bandwidth of PCR undergo dramatic changes, whereas when r continues to increase, PCR remains almost constant since there is no gap between the semicircle and square rings.

We also investigate the effects of the parameters l_1, w_1, and w_2 on PCR. Fig. 4(d) illustrates the impact of the parameter l_1 on PCR. Increasing the value of l_1 causes a redshift in the overall working band, which is the opposite of the trend observed in Fig. 4(a). When l_1 is increased, the period p decreases relatively, although the value of the parameter p actually remains the same. Consequently, the operating frequency band shifts towards lower frequencies, which is in line with the results shown in Fig. 4(a). When parameter l_2 is changed, its effect is similar to that of parameter r. In Fig. 4(e), an increase in w_1 has minimal impact on the low-frequency range of the PCR curve, while the high-frequency range experiences a linear blue shift. Similarly, in Fig. 4(f), an increase in w_2 induces a slight modification in the PCR curve's high-frequency range, while the low-frequency range experiences a blue shift. Specifically, the metal ring and square ring affect the high-frequency band and low-frequency band of the PCR curve, respectively. With the increase of both w_1 and w_2, the distance between the circular patch and square ring also increases, which inevitably weakens the resonance between the

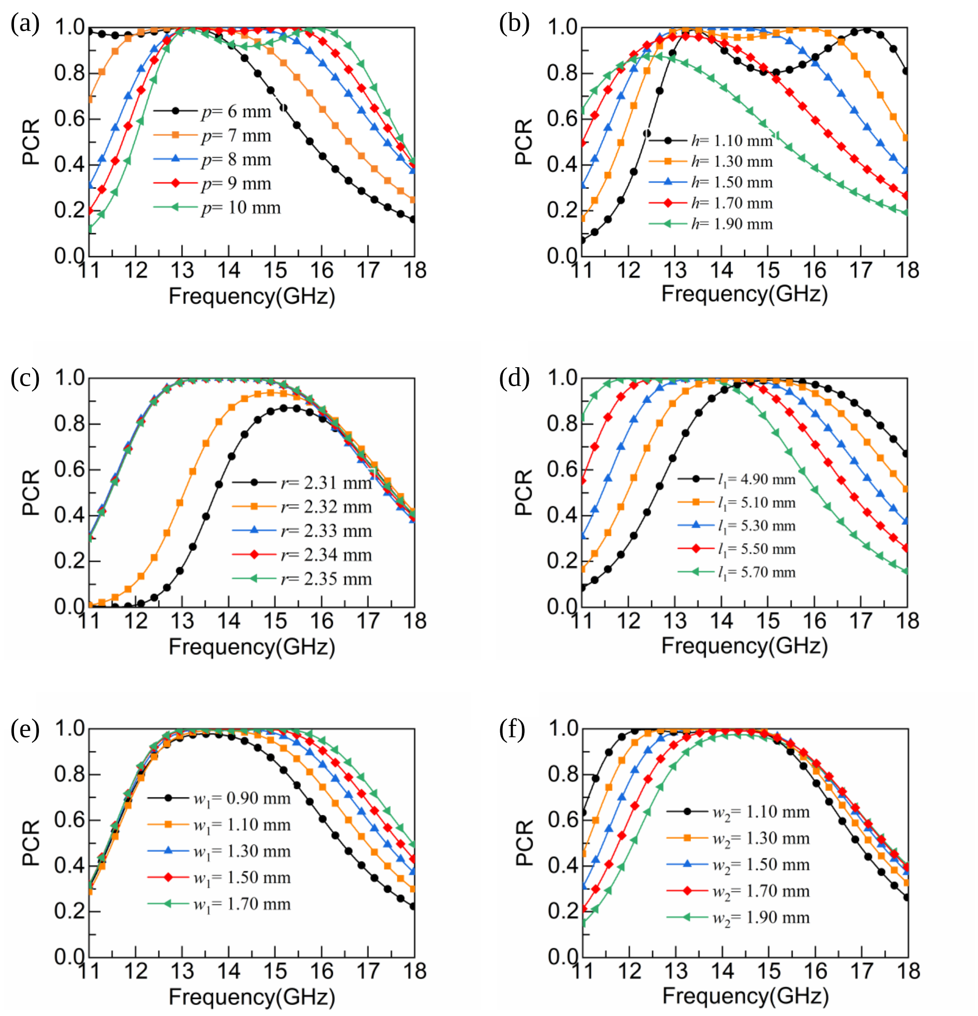

Figure 4. Effects of different parameters on PCR. (a) p, (b) t, (c) r, (d) l_1, (e) w_1, (f) w_2.

metallic components. Consequently, a blue shift occurs in the working frequency band, which aligns with the analysis results of parameter p and parameter l_1. These parameter analyses provide valuable guidelines for optimizing the parameters.

It is widely recognized that any electric field can be decomposed into two mutually orthogonal electric field components, and vice versa. The polarization conversion process of a y-polarized wave incident along the z-axis is investigated in this study. Fig. 5(a) depicts the operational principle of the polarizer. Assuming that the incident wave is a y-polarized (E_y^i) wave, and the reflected wave is x-polarized (E_x^r), the directions of their electric fields can be divided into components propagating along the u- and v-axes. The u- and v-axes correspond to a 45-degree rotation of the y-axis. Therefore, the following formula may be used to show the electric fields of the incident and reflected waves: [26]: $E_y^i = E_u^i e^{i(-kz-wt)}\hat{u} + E_v^i e^{i(-kz-wt)}\hat{v}$ for the incident electric field and $E_x^r = E_u^r e^{i(kz-wt+\phi_{uu})}\hat{u} + E_v^r e^{i(kz-wt+\phi_{vv})}\hat{v}$ for the reflected electric field, where E_u and E_v stand for, respectively, the u- and v-axis components of the electric field. The phase difference between E_u^r and E_v^r can be computed using $\varphi_{uv} = \varphi_{uu} - \varphi_{vv}$. We have $r_{uu} = r_{vv}$ and $\varphi_{uv} = 0$ or $\varphi_{uv} = \pm\pi$ when the incident wave is cross-polarized. Fig. 5(b) displays the phase discrepancies and the amplitude of the reflectance along the u and v directions. The amplitudes of the u and v axes are almost identical, and the phase difference is about 180° at 11.7–16.0 GHz. This implies that the incident y-polarized wave is cross-polarized.

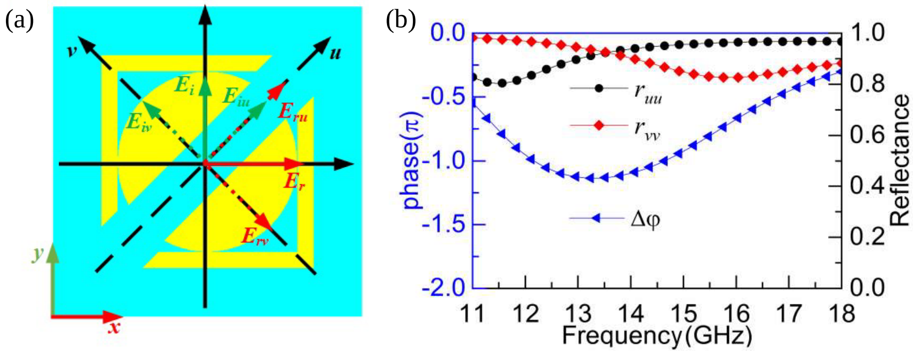

Figure 5. (a) The operational mechanism of the polarizer. (b) Simulation results of reflections and phase along u- and v-axes.

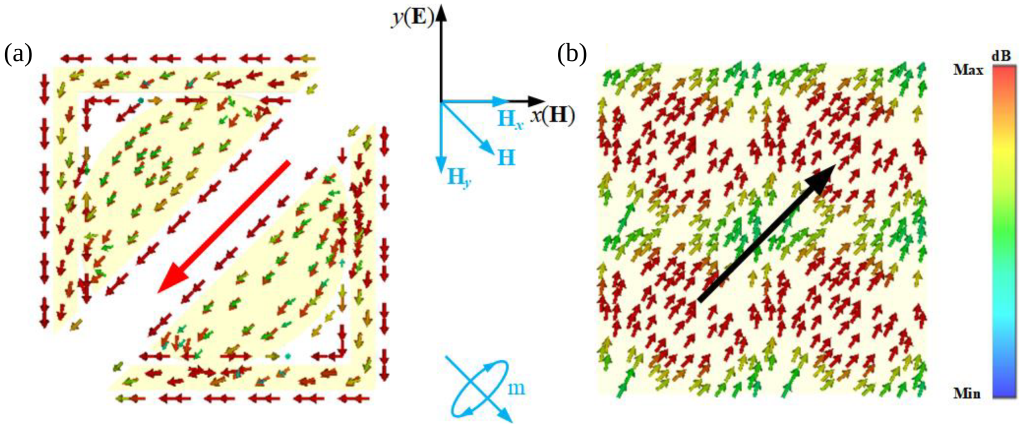

Figure 6. Surface current distribution at 13.7 GHz. (a) The upper layer, (b) the bottom layer.

We examine the surface current distribution of a linearly polarized wave at its resonance point of $f = 13.7\,\text{GHz}$, as depicted in Fig. 6, aiming to gain a deeper understanding of the fundamental physical mechanism underlying polarization deflection. The observations of of Figs. 6(a) and 6(b) represent the current distribution of the metal patches at $f = 13.7\,\text{GHz}$. It can be seen that the current along the red arrow of the top metal and the black arrow of the backplane form a closed loop to generate magnetic dipole ($\mathbf{m}$). The surface current generates a magnetic field in the lower right direction, which can be decomposed into mutually orthogonal components $\mathbf{H}_x$ and $\mathbf{H}_y$. $\mathbf{H}_x$ is orthogonal to the primary electric field ($\mathbf{E}$) and has no effect on polarization deflection, while $\mathbf{H}_y$ is parallel to the $\mathbf{E}$, resulting in a 90-degree polarization deflection.

In Table 1, we present a comparison between our proposed linear polarizer and other recent works, highlighting its superior polarization performance under wide-angle incidence in the Ku-band. The results demonstrate that our MS outperforms other designs in terms of its ability to manipulate and control polarization. In [27], the MS achieves a high PCR of up to 0.95 and a thickness of only 0.762 mm in two frequency bands, but its period is up to 23 mm, making it challenging to integrate. The study only analyzes its performance under normal incidence without considering oblique incidence. The MSs in [9] and [28] also have relatively small sizes, with the former maintaining a PCR of over 90% at incident angles from 0 to 30°, but its relative bandwidth is only 22.2%, and its dielectric substrate material is expensive FR-4. The latter achieves only 80% PCR under oblique incidence. The MS design proposed in [29] features a relatively wide relative bandwidth of 55.5%, but exhibits a lower PCR of only 80% and has a thickness of 4 mm. Furthermore, the MS design presented in [30] demonstrates a higher PCR in a dual frequency band, but its performance is limited under normal angle incidence, and it has larger dimensions. In contrast, our proposed mass spectrum utilizes FR-4 substrates, which are more cost-

Table 1. Comparative analysis with recent works.

Refs.	UCS (mm^3)	OB (GHz)	RB (%)	PCR (%)	IA (°)	substrate
[9]	$6 \times 6 \times 1.6$	12–18	40.0	80	0–45	FR-4
[27]	$23 \times 23 \times 0.762$	9.4–13.1 and 13.4–17.2	32.9 and 24.8	95	0	Rogers4725
[28]	$8 \times 8 \times 2$	12.0–15.0	22.2	90	0–30	F4-B
[29]	$10.5 \times 10.5 \times 4$	11.2–19.8	55.5	80	0	F4-B
[30]	$12 \times 12 \times 3$	4.4–5.3 and 9.4–13.6	18.6 and 36.5	86	0	FR-4
This work	$8 \times 8 \times 1.5$	12.0–16.0	28.6	90	0–45	FR-4

[1] UCS: unit cell size [2] OB: operating bandwidth [3] RB: relative bandwidth [4] IA: Incident angle

effective to process. Furthermore, it offers superior performance, including a wider relative bandwidth, higher PCR than previous designs, and improved functionality at various angles of incidence, all while maintaining a more compact size.

4. CONCLUSION

In conclusion, our proposed double-layer metasurface design offers a simple yet effective solution for achieving broadband linear cross-polarization conversion. The designed polarizer has achieved a PCR of over 90% in 12.0–16.0 GHz, with excellent polarization conversion efficiency even under wide-angle oblique incidence. The experimental results confirm the simulation ones. The mechanism of polarization conversion is successfully explained through magnetic dipole responses. Our proposed MS shows great potential for the development of high-performance polarization devices.

ACKNOWLEDGMENT

This work was supported by the Project of Science and Technology of Shaanxi (2021JM-395).

DECLARATIONS

The authors state no conflicts of interest regarding this article.

REFERENCES

1. Holloway, C. L., E. F. Kuester, J. A. Gordon, J. O'Hara, J. Booth, and D. R. Smith, "An overview of the theory and applications of metasurfaces: The two-dimensional equivalents of metamaterials," *IEEE Antennas Propag. Mag.*, Vol. 54, 10–35, 2012
2. Huang, X., X. Ma, X. Li, J. Fan, L. Guo, and H. Yang, "Simultaneous realization of polarization conversion for reflected and transmitted waves with bi-functional metasurface," *Sci. Rep.*, Vol. 12, 2368, 2022.
3. Song, Z. Y., Q. Chu, X. Shen, and Q. Liu, "Wideband high-efficient linear polarization rotators," *Front. Phys.*, Vol. 13, 137803, 2018.
4. Huang, X., X. Ma, H. Gao, L. Guo, and X. Li, "Ultra-wideband linear-polarization conversion metasurface with high-efficient asymmetric transmission," *Appl. Phys. A — Mater. Sci. Process.*, Vol. 129, 278, 2023.
5. Li, N., J. Zhao, P. Tang, and Y. Cheng, "Design of all-metal three-dimensional anisotropic metamaterial for ultrabroadband terahertz reflective linear polarization convertor," *Phys. Status Solidi*, Vol. 2300104, 1–7, 2023.

6. Habashi, A., C. Ghobadi, and J. Nourinia, "A dual-broadband h-shaped metasurface for cross-polarization and asymmetric transmission with high stable incidence angle," *AEU — Int. J. Electron. Commun.*, Vol. 143, 154021, 2021.
7. Wong, A. M. H. and G. Eleftheriades, "Perfect anomalous reflection with a bipartite huygens' metasurface," *Phys. Rev. X*, Vol. 8, 011036, 2018.
8. Feng, M., X. Tian, J. Wang, M. Yin, S. Qu, and D. Li, "Broadband abnormal reflection based on a metal-backed gradient index liquid slab: An alternative to metasurfaces," *J. Phys. D: Appl. Phys.*, Vol. 48, 245501, 2015.
9. Nguyen, T. Q. H., T. K. T. Nguyen, T. Q. M. Nguyen, T. N. Cao, H. L. Phan, N. M. Luong, D. T. Le, X. K. Bui, C. L. Truong, and D. L. Vu, "Simple design of a wideband and wide-angle reflective linear polarization converter based on crescent-shaped metamaterial for Ku-band applications," *Opt. Commun.*, Vol. 486, 126773, 2021.
10. Ding, F., Y. Chen, and S. I. Bozhevolnyi, "Gap-surface plasmon metasurfaces for linear-polarization conversion, focusing, and beam splitting," *Photonics Res.*, Vol. 8, 707–714, 2020.
11. Zheng, Q., C. Guo, and J. Ding, "Wideband metasurface-based reflective polarization converter for linear-to-linear and linear-to-circular polarization conversion," *IEEE Antennas Wirel. Propag. Lett.*, Vol. 17, 1459–1463, 2018.
12. Noishiki, T., R. Kuse, and T. Fukusako, "Wideband metasurface polarization converter with double-square-shaped patch elements," *Progress In Electromagnetics Research C*, Vol. 105, 47–58, 2020.
13. Yu, J., Q.-R. Zheng, B. Zhang, H. Jiang, and K. Zou, "Multifunction cross polarization converter based on ultra-thin transmissive chiral metasurface in C and X bands," *Progress In Electromagnetics Research M*, Vol. 109, 205–216, 2022.
14. Li, N., J. Zhao, P. Tang, and Y. Cheng, "Broadband and high-efficient reflective linear–circular polarization convertor based on three-dimensional all-metal anisotropic metamaterial at terahertz frequencies," *Opt. Commun.*, Vol. 541, 129544, 2023.
15. Ratni, B., A. De Lustrac, G. P. Piau, and S. N. Burokur, "Electronic control of linear-to-circular polarization conversion using a reconfigurable metasurface," *Appl. Phys. Lett.*, Vol. 111, 214101, 2017.
16. Fei, P., G. A. E. Vandenbosch, W. H. Guo, X. Wen, D. Xiong, W. Hu, Q. Zheng, and X. Chen, "Versatile cross-polarization conversion chiral metasurface for linear and circular polarizations," *Adv. Opt. Mater.*, Vol. 8, 2000194, 2020.
17. Long, F., S. Yu, N. Kou, C. Zhang, Z. Ding, and Z. Zhang, "Wideband and high-efficiency planar chiral structure design for asymmetric transmission and linear polarization conversion," *J. Appl. Phys.*, Vol. 127, 023104, 2020.
18. Cheng, Y., D. Yang, and X. Li, "Broadband reflective dual-functional polarization convertor based on all-metal metasurface in visible region," *Phys. B Condens. Matter*, Vol. 640, 414047, 2022.
19. Wang, X., J. Ding, B. Zheng, S. An, G. Zhai, and H. Zhang, "Simultaneous realization of anomalous reflection and transmission at two frequencies using Bi-functional metasurfaces," *Sci. Rep.*, Vol. 8, 1876, 2018.
20. Xu, J., R. Li, J. Qin, S. Wang, and T. Han, "Ultra-broadband wide-angle linear polarization converter based on H-shaped metasurface," *Opt. Express*, Vol. 26, 20913–20919, 2018.
21. Zhao, J., N. Li, and Y. Cheng, "All-dielectric inSb metasurface for broadband and high-efficient thermal tunable terahertz reflective linear-polarization conversion," *Opt. Commun.*, Vol. 536, 129372, 2023.
22. Gao, J., Y. Zhang, Y. Sun, and Q. Wu, "Ultra-wide band and multifunctional polarization converter based on dielectric metamaterial," *Materials (Basel)*, Vol. 12, 3857, 2019.
23. Wu, Y., S. Huang, L. Deng, C. Tang, X. Gao, S. Fang, and L. Qiu, "Dual-band linear polarization converter based on multi-mode metasurface," *Results Phys.*, Vol. 40, 105859, 2022.
24. Ahmed, F., M. Khan, and F. Tahir, "A multifunctional polarization transforming metasurface for C-, X-, and K-Band applications," *IEEE Antennas Wirel. Propag. Lett.*, Vol. 20, 2186–2190, 2021.

25. Wu, L. W., H. Ma, R. Wu, Q. Xiao, Y. Gou, M. Wang, Z. Wang, L. Bao, H. Wang, M. Ye, and T. Cui, "Transmission-reflection controls and polarization controls of electromagnetic holograms by a reconfigurable anisotropic digital coding metasurface," *Adv. Opt. Mater.*, Vol. 8, 2001065, 2020.
26. Lin, B. Q., J. Guo, P. Chu, W. Huo, Z. Xing, B. Huang, and L. Wu, "Multiple-band linear-polarization conversion and circular polarization in reflection mode using a symmetric anisotropic metasurface," *Phys. Rev. Appl.*, Vol. 9, 24038, 2018.
27. Su, J., Y. Guo, X. Chen, and W. Zhang, "A dual-wideband polarization-insensitive linear polarization converter based on metasurface," *Progress In Electromagnetics Research M*, Vol. 108, 213–222, 2022.
28. Yuan, L., L. Hou, and Z. Zhang, "Triple-band highly efficient multi-polarization converter based on reflective metasurface," *Progress In Electromagnetics Research M*, Vol. 102, 127–135, 2021.
29. Zhang, Z., X. Cao, J. Gao, and S. Li, "Broadband metamaterial reflectors for polarization manipulation based on cross/ring resonators," *Radioengineering*, Vol. 25, 436–441, 2016.
30. Huang, X., H. Yang, D. Zhang, and Y. Luo, "Ultrathin dual-band metasurface polarization converter," *IEEE Trans. Antennas Propag.*, Vol. 67, 4636–4640, 2019.